2018 IEEE International Conference on Robotics and Automation (ICRA)
May 21-25, 2018, Brisbane, Australia

Extended Kalman filter-based 3D active-alignment control for LED communication

Pratap Bhanu Solanki and Xiaobo Tan

Abstract— **LED-based optical communication is emerging as a low-cost, high-data-rate alternative to the traditional acoustics mode of underwater communication. However, it is challenging to establish and maintain Line-Of-Sight (LOS) between the receiver and the transmitter, especially when such systems are used by mobile robots. Hence, there is a need for an active alignment system that enables the receiver to constantly align itself towards the direction of the transmitting device. In this paper, we propose and implement an active alignment control system capable of tracking a transmitting source moving in the three-dimensional (3D) space. An extended Kalman filter is used to estimate the components of the angle between the receiver orientation and the receiver-transmitter line. Using the estimate, a proportional-integral (PI) controller is implemented to adjust the receiver orientation. The algorithm uses one measurement of the light intensity from a single photo-diode, where successive measurements are obtained via a circular scanning technique. The amplitude of the scanning is adapted to the alignment performance, to achieve a sound trade-off between estimation accuracy, signal strength, and energy consumption. Simulation and experimental results are presented to illustrate the effectiveness of the proposed approach.**

I. INTRODUCTION

Underwater wireless communication is necessary between autonomous underwater robots deployed for collaborative tasks, such as environmental monitoring, oil/gas exploration, and assisting human divers, etc. Due to the heavy attenuation of radio frequency signals in water [1], currently, acoustic communication is the prevailing method for underwater robots to communicate with each other and/or the base stations. However, acoustic communication suffers from the drawbacks of low data rates, high latency, and high power consumption [2]. Recently, light-emitting diode (LED)-based optical communication has been proposed as a promising low-cost, high-data-rate, low-power solution for low-to-medium range underwater data transfer applications [3], [4], [5]. A number of studies focused on increasing the communication range and data rates of LED communication systems have been reported. For example, Brundage designed an optical communication system using a Titan blue lighting LED [6], which performed error-free communication over 1 Mbps at distances up to 13 m. Doniec and Rus demonstrated a bidirectional underwater wireless communication system called AquaOptical II [7], which used 18 Luxeon Rebel LEDs and an avalanche photo-diode (APD) and operated over a distance of 50 m at a data rate of 4 Mbps.

Pratap Bhanu Solanki and Xiaobo Tan are with the Department of Electrical and Computer Engineering, Michigan State University, 428 S Shaw Lane, East Lansing, Michigan 48824, United States of America prabhanu@egr.msu.edu, xbtan@egr.msu.edu

Due to the high directionality of the light signals, an inherent challenge associated with wireless LED optical communication is to establish and maintain close-to-line-of-sight links. For many potential applications involving underwater robots, maintaining a line-of-sight (LOS) is difficult due to movement of the underlying robotic platform caused by propulsion or ambient disturbances. Several approaches have been proposed to address the LOS requirement in optical communication systems. Pontbriand *et al.* used large-area photomultiplier tubes, to increase the field of view of the receiver [8]. Multiple LEDs and/or multiple photo-diodes have been used to avoid the need for active pointing during optical-communication [7], [9], [10], [11], [12]. Use of quadrant detectors [13], [14] has also been reported for optical beam tracking, where four photo-receivers were arranged in a plane, facing the same direction. Most of the former systems achieved the line of sight through redundancy in transmitters and/or receivers, which resulted in a larger footprint, higher cost, and higher complexity.

In our previous work [15], we implemented an active alignment control scheme for LED communication systems, where measurements from a single photo-diode were used. The system was able to track a light transmitter, moving in a 2-dimensional (2D) space. However, in a practical underwater scenario, the robots move in a 3D space and there is a need for active alignment control that could establish and maintain the LOS with a transmitter moving in the 3D space. In this work, we propose and implement an active alignment control to maintain the LOS in the 3D space. This paper is a significant extension of our earlier work [16], which was limited to a preliminary simulation study. In particular, this paper presents improved algorithms on both estimation and control, and more importantly, the design and implementation of the active alignment control system, and evaluation in extensive simulation and experimentation. For example, instead of using three measurements in an iteration, we now demonstrate that a single measurement is sufficient for guaranteeing the observability of the system if the next two successive measurements, along with the present measurement, are not taken from coplanar directions. This has simplified the overall implementation of the algorithm and reduced the computational cost, which is crucial for the on-board implementation of the algorithm.

A circular scanning technique is used to ensure the system observability in successive light intensity measurements, which are used by the EKF-based algorithm to estimate the orientation angles with respect to the transmitter. A PI control algorithm then uses these estimates to generate

the motor commands to orient the receiver in the desired transmitter-receiver line. In addition, to save energy and maximize signal strength at the steady state, the amplitude of the circular scanning is adapted according to the alignment performance: starting with a high scanning amplitude so that the successive measurements are distinguishable to enable good estimation accuracy and then decreasing the amplitude to reduce the energy consumption and attain maximum light intensity when the steady state is reached. Both simulation and experimental results verify the efficacy of the proposed algorithm.

The rest of the paper is organized as follows. In Section II, the hardware implementation of the 3D alignment control mechanism is first described, followed by the modeling of the received light intensity in Section III. The model is then used to develop a state-space dynamic model for the estimation algorithm development. In Section IV the estimation and tracking control algorithms are described. Simulation setup and results are presented in Section V, while experimental setup and results are discussed in Section VI. Finally, concluding remarks are provided in Section VII.

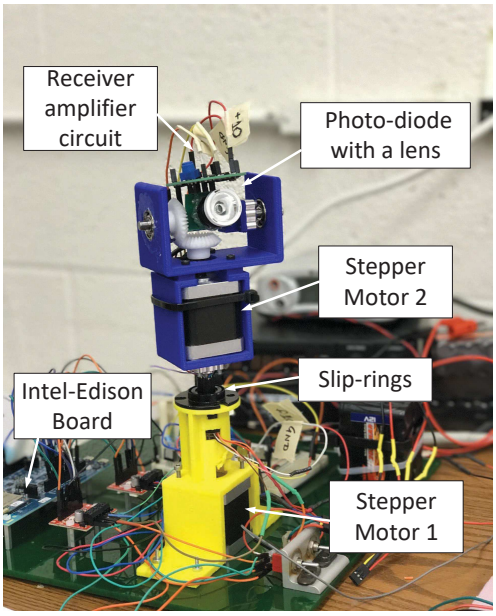

Fig. 1. Experimental setup, where the receiver photo-diode with two-DOF active orientation adjustment is shown.

II. SYSTEM SETUP

In this section, we describe the experimental setup used in our work. We first discuss the components of our receiver system. A photo-diode from Advanced Photonix (part number PDB-V107) is chosen for the receiver, and it has high quantum efficiency at 410 nm, low dark current, and fast rise time (20 ns). This makes it a suitable device for communication with bandwidth on the order of 100 KHz to 1 MHz. Fig. 1 shows the mechanism for adjusting the receiver orientation in the 3D space. The mechanism consists of two stepper motors: the first one at the base, also referred to as the base stepper motor, is used for adjusting the azimuthal orientation, while the second stepper motor, through a miter bevel gear assembly, is used for adjusting the elevation of the receiver orientation. This configuration maintains the low moment of inertia of the rotating stage and minimizes the load on the base stepper motor, which improves overall efficiency as compared to the alternative, where the stepper motor axes are perpendicular to each other. A lens is mounted on the photo-diode to increase the field of view. An Intel Edison microprocessor board is used for the required on-board computation. Slip rings are also used for a smooth transmission of power and electrical signals between the rotating stage and the base stage. For the transmitter, we use an off-the-shelf blue LED (Cree XR-E Series LED from Cree Inc) which provides 30.6 lumens at 1 A.

III. MODELING

In this section, we briefly, discuss the light intensity model and then formulate the state-space model for an estimation problem, where a scenario of two robots is considered.

A. Light signal strength model

The model adopted here largely follows [17] with minor adjustments to suit the experimental prototype used in this paper. The model takes into account all stages of the transmitter and receiver circuits, including LED, lens, photo-diode, and amplifiers. The model mainly describes the effect of relative position and orientation between the transmitter and the receiver on the signal strength. Fig. 2 illustrates the two 3D coordinate systems, referred to as the base frame $(o - x'y'z')$ and the receiver frame $(o - xyz)$, respectively, and defines all the variables of interest associated with our analysis. The receiver's location is chosen as the origin of the coordinate systems. The rotational axis of the base stepper motor is considered as the y' axis (the superscript prime is used for the base coordinate system). The line joining the receiver and the transmitter is chosen as the x axis of the receiver frame. Now, the axis perpendicular to the plane containing x and y' axes is defined as z and z' axis for the respective coordinate systems. The remaining y-axis for the receiver frame and the x'-axis for the base frame are inferred by the right-hand rule. The parameter d is the distance between the receiver and the transmitter. The transmission angle γ is the angle between the transmitter and the transmitter-receiver line, which is also termed as the communication line in this paper. The angles, θ and ϕ, are the two orthogonal components of the angle made by the receiver's normal with the communication line, where ϕ represents the yaw and θ represents the pitch orientation in the receiver frame. Using a spatial intensity curve I_γ of the transmitter LED, which represents the light intensity at a unit distance for different transmitter angles, the intensity at points with same radial distance from the transmitter can be calculated if the intensity at $\gamma = 0^\circ$ is known. The intensity of light reaching a spatial point at a distance d and at an angle γ can be summarized as

$$E_\gamma(d) = I_\gamma e^{-cd}/d^2 \tag{1}$$

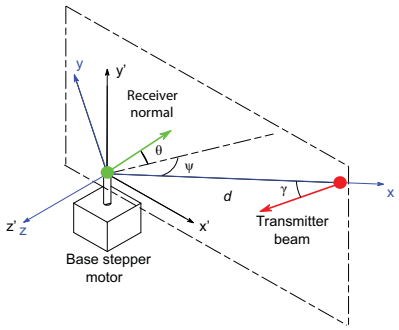

Fig. 2. Illustration of two 3D coordinate systems and the variables associated with the relative position and orientation between the transmitter and the receiver.

where c is the attenuation coefficient for the medium in which the light is transmitted. Considering the effect of the receiver's orientation and area, the final power at the receiver can be written as:

$$P_{\text{in}} = E_\gamma(d) A_0 f(\phi, \theta) \tag{2}$$

where A_0 denotes the detector area and $f(\phi, \theta)$ characterizes the dependence of the received light intensity on the incidence angles ϕ and θ. The term $f(\phi, \theta)$ is a setup-dependent term. For our setup, we have found the function $f(\phi, \theta)$ using Gaussian curve fitting of normalized measurement data (Fig. 3) that were collected for different orientations of the receiver. It is observed that the measurement data is circularly symmetric about the peak. Henceforth, for practical purposes and simplicity in analysis, $f(\phi, \theta)$ can be approximated by a product of two one dimensional Gaussian-type functions $g(\phi)$ and $g(\theta)$:

$$f(\phi, \theta) = g(\phi) g(\theta) \tag{3}$$

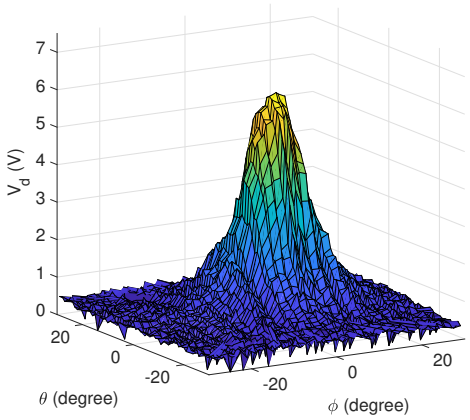

Fig. 3. Light intensity data for estimation of $f(\phi, \theta)$.

where $g(\cdot)$ is a bimodal Gaussian function obtained by curve fitting [16]. The full signal strength model can be summarized as

$$V_d = C I_\gamma e^{-cd} g(\phi) g(\theta) / d^2 \tag{4}$$

where V_d is the voltage signal and C is a constant of proportionality, which depends on the area of receiver photodiode and various parameters associated with the filter and amplifier circuits.

B. State-space problem formulation

From Fig. 2 and Eq. (4), we can see that there are four independent variables, γ, d, ϕ and θ, that characterize the received signal strength. One could take these four variables as the states to be estimated by the system, and then try to drive them towards their desired values through control. However, often times the underlying robotic platforms are engaged in other tasks and may not constrain or modify their motions to accommodate communication. What is much more practical is to control the receiver's orientation (ϕ and θ), since it is a completely local decision due to the independent rotation base for the transceiver. In a two-way communication setting, since the transmitter and the receiver on each robot are pointing in the same direction, adjusting ϕ and θ to zero on each robot automatically aligns each transmitter with the line connecting two robots. In light of this discussion, we can combine terms involving γ and d in a single variable and define the state variables as

$$\mathbf{x} = \begin{bmatrix} x_1 \\ x_2 \\ x_3 \end{bmatrix} \triangleq \begin{bmatrix} C I_\gamma e^{-cd}/d^2 \\ \phi \\ \theta \end{bmatrix} \tag{5}$$

The value of $\mathbf{x}$ is dependent on the distance and relative orientation between the receiver and the transmitter. In a typical scenario, the receiver does not have information about how the transmitter and its underlying robotic platform move. So we will assume that the relative dynamics between the two communicating robots is slow enough that it can be captured with Gaussian noises. In particular, the dynamics of the states defined in (5) can be represented in the discrete-time domain as

$$\mathbf{x}_k = \begin{bmatrix} x_{1,k} \\ x_{2,k} \\ x_{3,k} \end{bmatrix} = \begin{bmatrix} x_{1,k-1} + w_{1,k-1} \\ x_{2,k-1} + u_{2,k-1} + w_{2,k-1} \\ x_{3,k-1} + u_{3,k-1} + w_{3,k-1} \end{bmatrix} \tag{6}$$

where $w_{1,k}$, $w_{2,k}$ and $w_{3,k}$ are the process noises, assumed to be independent, white, Gaussian noises. These noise terms, up to some extent can account for the slow dynamics of $\mathbf{x}_k$, which are not modeled explicitly. The terms $u_{2,k}$ and $u_{3,k}$ are the control inputs through which the receiver's orientation is changed. These two inputs are related to motor commands by a rotational transformation, which is discussed later. The kth measurement $V_{d,k}$ can be expressed in terms of the state variables, where an additive white Gaussian noise v_k, assumed to be independent from the process noises, is included:

$$V_{d,k} = x_{1,k} g(x_{2,k}) g(x_{3,k}) + v_k \tag{7}$$

Given the measurement, the goal is to estimate $x_{1,k}$, $x_{2,k}$ and $x_{3,k}$ based on which the control term $\mathbf{u_k} = [u_{2,k}, u_{3,k}]^T$ is designed, to drive x_2 and x_3 towards $0°$, which is the orientation with the maximum light intensity.

IV. ESTIMATION AND ALIGNMENT ALGORITHMS

In this section, we first explore the observability of our system and then introduce the circular scanning technique,

followed by the design of a feedback controller and the discussion on the implementation of the EKF algorithm.

A. Observability of the system

Given that the measurement model (7) is nonlinear, an extended Kalman filter [18] is explored for solving the estimation problem. From the (linear) state equation (6), define

$$A = \begin{bmatrix} 1 & 0 & 0 \\ 0 & 1 & 0 \\ 0 & 0 & 1 \end{bmatrix}, \; B = \begin{bmatrix} 0 & 0 \\ 1 & 0 \\ 0 & 1 \end{bmatrix} \tag{8}$$

Then the system dynamics can be written as:

$$\mathbf{x}_k = A\mathbf{x}_{k-1} + B\mathbf{u}_{k-1} + \mathbf{w}_{k-1} \tag{9}$$

with $\mathbf{w}_k = [w_{1,k}, w_{2,k}, w_{3,k}]^T$. Denoting the system's linearized output matrix at the kth time instant as $C_k \triangleq C(\mathbf{x}_k)$, one can express the observability matrix at that time instant as [18]

$$\mathcal{O}_k = \begin{bmatrix} C_k \\ C_{k+1}A \\ C_{k+2}A^2 \end{bmatrix} = \begin{bmatrix} C_k \\ C_{k+1} \\ C_{k+2} \end{bmatrix} \tag{10}$$

Therefore, for the system to be observable, $\mathcal{O}_k$ needs to be non-singular. One of the possible ways to ensure this criterion is to make the three consecutive C_k's to be linearly independent with each other, which implies that we need at least 3 consecutive independent measurements of light intensity. In this situation, the measurements would be independent if they are taken from three non-planar orientations of the receiver. Hence, we introduce a circular scanning technique, where the two motors of the receiver mechanism are commanded to move in such a way that the direction of the photo-diode moves in a circular manner centered around a mean orientation. This mean orientation, which is what the control input modulates, is (x_2, x_3).

The scanning pattern design is based on two parameters: scanning amplitude δ_r and angular step δ_ψ (see Fig. 4), where δ_r regulates the angular distance of the measurement points from the mean angular position, and the subscript r denotes that it is the radius of the circular scanning pattern. The notation δ_ψ accounts for the angular displacement between the two successive measurement points. The relative angular position of a measurement point with respect to the mean (x_2, x_3) at the kth instant is defined as ψ_k, which has two orthogonal components α_k and β_k as shown in (11):

$$\begin{cases} \psi_k = \psi_{k-1} + \delta_\psi \\ \beta_k = \delta_r \cos(\psi_k), \\ \alpha_k = \delta_r \sin(\psi_k) \end{cases} \tag{11}$$

Fig. 4 illustrates the scanning technique. The receiver photo-diode moves around the mean (x_2, x_3) in successive steps of size δ_ψ. The measurement is taken at each ψ_k and is considered as our output $\mathbf{y}_k$:

$$\mathbf{y}_k = x_{1,k} g(x_{2,k} + \beta_k) g(x_{3,k} + \alpha_k) + v_k \tag{12}$$

Fig. 5 illustrates the overall flow of our estimation and control method. The estimates $\hat{x}_2$ and $\hat{x}_3$ and their integral states are fed to a PI controller to generate the control terms. The control terms with the addition of the scanning terms are translated to the base coordinate system using a rotational transformation. The motor commands are generated using these transformed terms.

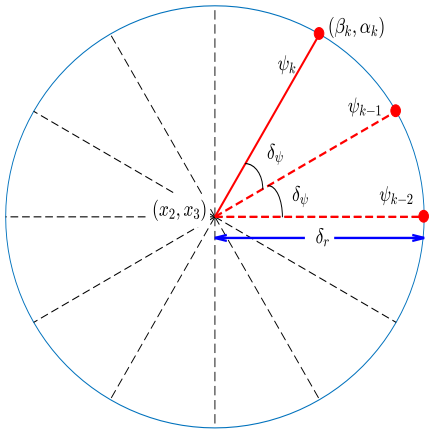

Fig. 4. Illustration of the circular scanning sequence, with mean (x_2, x_3) and the last three angular positions of scanning ψ_k, ψ_{k-1} and ψ_{k-2}

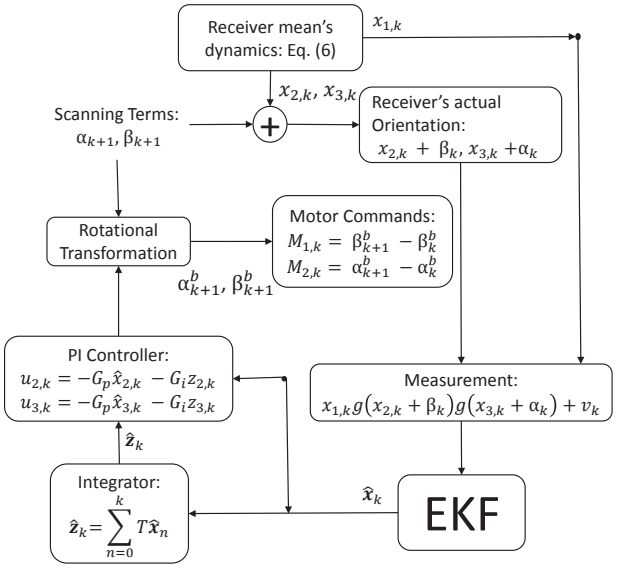

Fig. 5. Block diagram illustrating the flow of the proposed method.

B. Design of a feedback controller

A PI controller will be used to drive the receiver towards the transmitter. While in implementation the EKF-based state estimates will be used as feedback, here we assume direct state feedback in order to analyze the constraints on the controller gains for ensuring stability. The controllers are written as

$$\begin{cases} u_{2,k} = -G_P x_{2,k} - G_I z_{2,k} \\ u_{3,k} = -G_P x_{3,k} - G_I z_{3,k} \end{cases} \tag{13}$$

where $z_{2,k}$ and $z_{3,k}$ are the integrals of states $x_{2,k}$ and $x_{3,k}$ respectively, defined by:

$$z_{i,k} \triangleq \sum_{n=0}^{k-1} T x_{i,n} = z_{i,k-1} + T x_{i,k-1}, \; i \in \{2, 3\} \tag{14}$$

where T is the sampling time. G_P and G_I are positive constants which account for the proportional and integral

gains of the controller, respectively. Given the symmetry over x_2 and x_3, the same PI parameters are used for both of the control terms in Eq. (13). The closed-loop system is:

$$\begin{bmatrix} x_{1,k} \\ x_{2,k} \\ z_{2,k} \\ x_{3,k} \\ z_{3,k} \end{bmatrix} = \begin{bmatrix} 1 & 0 & 0 & 0 & 0 \\ 0 & 1-G_P & -G_I & 0 & 0 \\ 0 & T & 1 & 0 & 0 \\ 0 & 0 & 0 & 1-G_P & -G_I \\ 0 & 0 & 0 & T & 1 \end{bmatrix} \begin{bmatrix} x_{1,k-1} \\ x_{2,k-1} \\ z_{2,k-1} \\ x_{3,k-1} \\ z_{3,k-1} \end{bmatrix} \tag{15}$$

Since the states are decoupled, one of the eigenvalues would be 1 (corresponds to state x_1, which is not controllable) and the other four would be repeated eigenvalues of the 2×2 submatrix highlighted above (say A'), which would be the roots of Eq. (16):

$$\lambda^2 - (2 - G_P)\,\lambda + (1 - G_P + G_I T) = 0 \tag{16}$$

For the subsystem to be stable, the PI parameters are chosen in such a way that both eigenvalues of the A' matrix lie inside the unit circle, centered at the origin of a complex plane.

C. Implementation of extended Kalman filter

With the dynamics equation (6) and the measurement equation (12), an extended Kalman filter (EKF) can be implemented. The complete algorithm is explained as follows.

There are three covariance matrices, namely, P, Q and R, associated with an EKF. P is the conditional error covariance matrix and P^f represents the forecast of the covariance matrix. Q is the process noise covariance matrix, and R is the measurement noise covariance. At step k,

1) **Prediction phase** : Both state estimates ($\hat{x}$) and error co-variance matrix (P^f) are predicted:

$$\hat{\mathbf{x}}_k^f = \begin{bmatrix} \hat{x}_{1,k} \\ \hat{x}_{2,k} \\ \hat{x}_{3,k} \end{bmatrix} = \begin{bmatrix} \hat{x}_{1,k-1} \\ \hat{x}_{2,k-1} + u_{2,k-1} \\ \hat{x}_{3,k-1} + u_{3,k-1} \end{bmatrix} \tag{17}$$

$$P_k^f = A P_{k-1} A^T + Q \tag{18}$$

where $\hat{x}_{m,k}^f$ denotes the estimate of the mth state at kth interval and superscript f stands for 'forecast'.

2) **Estimated output**:
From (12), we get

$$\hat{\mathbf{y}}_k = \hat{x}_{1,k} g(\hat{x}_{2,k} + \beta_k) g(\hat{x}_{3,k} + \alpha_k) \tag{19}$$

Now the C matrix can be computed as:

$$C_k = \frac{\partial h(\hat{\mathbf{x}}_k^f)}{\partial \hat{\mathbf{x}}_k^f} = \begin{bmatrix} C_{k,1} & C_{k,2} & C_{k,3} \end{bmatrix} \tag{20}$$

where,

$$\begin{cases} C_{k,1} = g(\hat{x}_{2,k} + \beta_k) g(\hat{x}_{3,k} + \alpha_k) \\ C_{k,2} = \hat{x}_{1,k} g'(\hat{x}_{2,k} + \beta_k) g(\hat{x}_{3,k} + \alpha_k) \\ C_{k,3} = \hat{x}_{1,k} g(\hat{x}_{2,k} + \beta_k) g'(\hat{x}_{3,k} + \alpha_k) \end{cases} \tag{21}$$

with $g'(\cdot)$ being the derivative of $g(\cdot)$.

3) **Update/analysis phase**:

$$\begin{cases} K_k = P_k^f C_k^T (C_k P_k^f C_k^T + R)^{-1} \\ \hat{\mathbf{x}}_k = \hat{\mathbf{x}}_k^f + K_k(\mathbf{y}_k - \hat{\mathbf{y}}_k) \\ P_k = (I - K_k C_k) P_k^f \end{cases} \tag{22}$$

It is to be noted that P_k and $\hat{\mathbf{x}}_k$ without any superscripts denote the updated values after the analysis phase.

4) Now, the control terms are computed as

$$\begin{cases} u_{2,k} = -G_P \hat{x}_{2,k} - G_I \hat{z}_{2,k} \\ u_{3,k} = -G_P \hat{x}_{3,k} - G_I \hat{z}_{3,k} \end{cases} \tag{23}$$

where the terms $\hat{z}_{2,k}$ and $\hat{z}_{3,k}$ are the integrals of the estimates $\hat{x}_{2,k}$ and $\hat{x}_{2,k}$, respectively.

D. Generation of motor commands

It is to be noted that the above analysis is done in a local coordinate system (the receiver frame) and we need to translate those control terms to the base coordinate system to generate motor commands. Let θ_k^b be the elevation of the photo-diode's mean orientation (center of the scanning pattern, which is known) at the kth iteration. The superscript b stands for the base coordinate system. The translation of the control terms to the base coordinate system is as follows:

$$\begin{cases} u_{2,k}^b = \arctan 2(\cos(u_{3,k}) \sin(u_{2,k}), \cos(u_{3,k}) \\ \qquad \cos(u_{2,k}) \cos(\theta_k^b) - \sin(u_{3,k}) \sin(\theta_k^b)) \\ u_{3,k}^b = \arcsin(\cos(u_{3,k}) \cos(u_{2,k}) \sin(\theta_k^b) + \sin(u_{3,k}) \\ \qquad \cos(\theta_k^b)) - \theta_k^b \end{cases} \tag{24}$$

Now the new elevation and azimuthal angles of the photo-diode's mean position in the base coordinate system are

$$\begin{cases} \theta_{k+1}^b = \theta_k^b + u_{3,k}^b \\ \phi_{k+1}^b = \phi_k^b + u_{3,k}^b \end{cases} \tag{25}$$

The actual photo-diode's orientation consists of the scanning terms as well. Translating the scanning terms to the base coordinate system results in the actual net orientation of the receiver:

$$\begin{cases} \beta_{k+1}^b = \arctan 2(\cos(\alpha_{k+1}) \sin(\beta_{k+1}), \cos(\alpha_{k+1}) \\ \qquad \cos(\beta_{k+1}) \cos(\theta_{k+1}^b) - \sin(\alpha_k) \sin(\theta_k^b)) + \psi_{k+1} \\ \alpha_{k+1}^b = \arcsin(\cos(\alpha_{k+1}) \cos(\beta_{k+1}) \sin(\theta_{k+1}^b) \\ \qquad + \sin(\alpha_{k+1}) \cos(\theta_{k+1}^b)) \end{cases} \tag{26}$$

where β_{k+1}^b and α_{k+1}^b are the yaw and pitch orientations of the photo-diode respectively. The final commands sent to the motors would be the difference of the next computed orientation with the current orientation:

$$\begin{cases} M_{1,k} = \beta_{k+1}^b - \beta_k^b \\ M_{2,k} = \alpha_{k+1}^b - \alpha_k^b \end{cases} \tag{27}$$

Furthermore, some additional adjustments have been made to improve the performance of the method. For instance, instead of activating the control commands from the very

beginning when the estimates have relatively large errors, the control is activated when the confidence about the estimates is high enough.In particular, a normalized filtered error function for the measurement is used as a metric to indicate the confidence of the estimator:

$$e_k = \frac{1}{3}\sum_{i=k-2}^{k}\frac{y_i - \hat{y}_i}{y_i} \tag{28}$$

A lower value of e_k indicates the high confidence on the estimates, so, the controller is activated when the error e_k is less than a certain threshold (0.3 is used in this work). In addition, an adaptive scanning approach is used, which is discussed in the next section.

V. SIMULATION RESULTS

The algorithm discussed is simulated in MATLAB. All the parameters related to the simulation implementation are listed in Table I. To explore the effects of unknown slow dynamics, a constant disturbance term κ is introduced in the dynamics of both x_2 and x_3. This disturbance is unknown to the EKF and emulates the practical scenario of the transmitter revolving around the receiver while facing the receiver. The simulated dynamics is thus

$$\begin{bmatrix} x_{1,k} \\ x_{2,k} \\ x_{3,k} \end{bmatrix} = \begin{bmatrix} x_{1,k-1} + w_{1,k-1} \\ x_{2,k-1} + u_{2,k-1} + \kappa T + w_{2,k-1} \\ x_{3,k-1} + u_{3,k-1} + \kappa T + w_{3,k-1} \end{bmatrix} \tag{29}$$

TABLE I
PARAMETERS USED IN SIMULATION.

Parameter	Value	Description
$\hat{x}_0^f$	$[3,0,0]^T$	Initial value of the estimates
P_0^f	diag([1, 10, 10])	Initial error-covariance matrix
Q_{sys}	diag([0.01, 0.1, 0.1])	System's process noise-covariance matrix
Q	diag([0.1, 1, 1])	EKF's process noise-covariance matrix
R_{sys}	0.1	System's measurement noise-covariance matrix
R	1	EKF's measurement noise-covariance matrix
$[G_P, G_I]$	[0.5, 0.1]	PI controller gains
δ_r	7	Scanning amplitude
$[\delta_l, \delta_l]$	[2,10]	Scanning amplitude limits
δ_ψ	30	Scanning angular step-size
T	80 ms	Sampling time

Fig. 6 illustrates a simulation run in angular coordinates of x_2 and x_3, when the disturbance κ is 1 $^\circ$/s. Here, as per our definition, the transmitter is at the origin. The blue squares denote the mean of the scans and the green trajectory represents the net estimated orientation of the receiver with the scanning terms included. Fig. 7 shows the evolution of the states and the estimates in the course of the EKF run. It can be observed that it takes about 10 seconds for the estimates to converge to true values, and once this is achieved, the controller shifts the scanning circle towards the transmitter, which is situated at the origin. The receiver's orientation stays around the origin despite the constant disturbance. Moreover, we can also observe that although the maximum possible intensity is 5 V (true value of x_1), the intensity measurements and its estimate oscillate about the mean of 3.5 V. This loss in intensity is because of the scanning motion. This loss in intensity can be critical at the time of actual communication, as lower light intensity results in lower signal to noise ratio (SNR) and could result in a higher bit error rate.

To avoid such scenarios and minimize the power consumed in the scanning, we introduce an adaptive scanning technique. Here, the normal scanning amplitude is made proportional to the normalized filtered error e_k:

$$\delta_{r,k} = \max\left(\delta_l, \min\left(10e_k, \delta_h\right)\right) \tag{30}$$

where δ_l and δ_h denote the lower and upper bounds of the scanning amplitude, respectively. Due to the requirement of three independent measurements from the observability criterion, the scanning amplitude cannot be made zero. Fig. 8

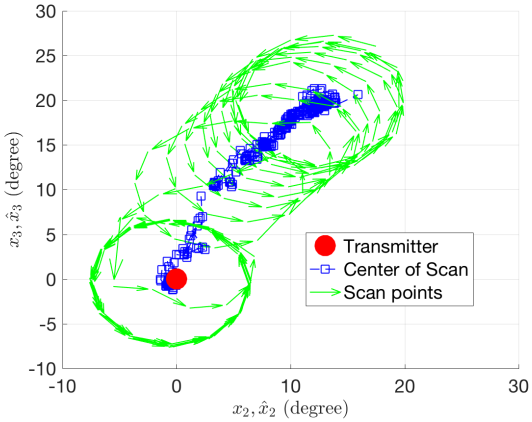

Fig. 6. Illustration of the simulation run on angular coordinates (x_2,x_3) with a constant scanning amplitude $\delta_r = 7^\circ$ under a constant disturbance $\kappa = 1^\circ/\text{s}$.

shows plots of a simulation run with the implementation of adaptive scanning. It can be seen that once the convergence is achieved, the scanning amplitude goes to its minimum value and remains there unless the error e_k increases due to some external disturbance. The steady state light intensity measurement is also increased to 95% of the maximum available intensity.

VI. EXPERIMENTAL RESULTS

In this section, we verify the efficacy of our algorithm by implementing it on the hardware setup discussed in Section II. The transmitter is mounted on a static clamp. Similar to the simulation, the artificial disturbance κ, is also implemented on the on-board program, to emulate the unknown relative angular motion between the receiver and the transmitter. When no control is implemented, this disturbance will rotate the receiver away from the transmitter-facing direction. For the initial condition, the receiver is kept at an angle of about 30 degrees from the transmitter-facing direction. Fig. 9 shows the evolution of the estimated

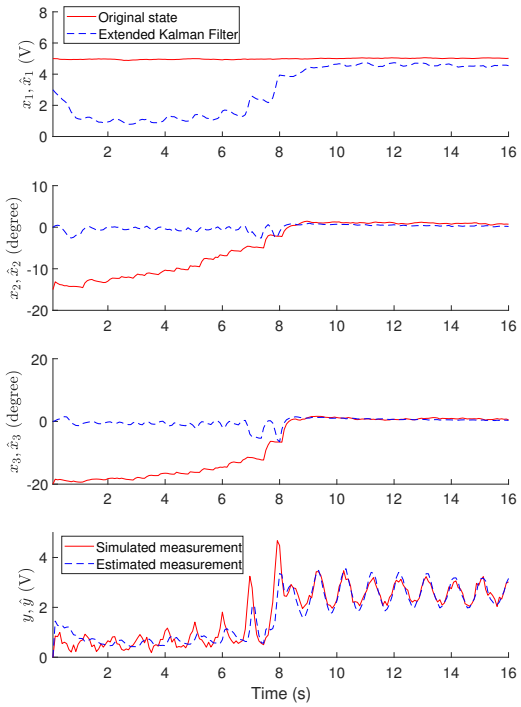

Fig. 7. Simulation results corresponding to Fig 6.

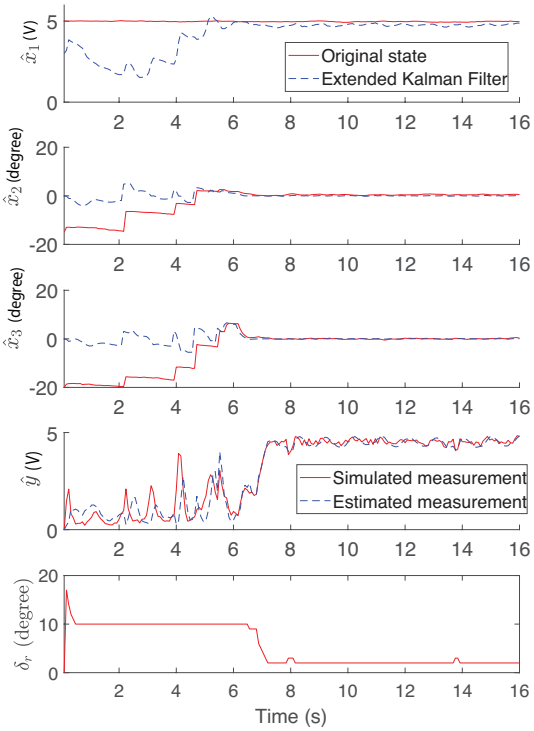

Fig. 8. Simulation results with adaptive scanning amplitude and disturbance $\kappa = 1^\circ/s$.

states and the intensity measurement. Since we do not have access to the true values of the state (it is possible to determine the true states by using some external motion-tracking system but that is beyond the scope of this work), the convergence cannot be directly verified. However, it can be seen that $\hat{x}_1$ reaches a steady state value in about 15 seconds and slightly oscillates about it. Similarly, $\hat{x}_2$ and $\hat{x}_3$ settle to the neighborhood of zero. Moreover, the measurement and its estimate both start from some low values and then oscillate around higher steady-state values. During the experiment, it is visually observed that the center of the scanning movement starts facing the transmitter after some time. Hence, it is reasonable to conjecture that the estimates have converged to the neighborhood of the actual states and an alignment with the transmitter direction is achieved. Furthermore, unlike what is observed in simulation, there are appreciable oscillations in the estimated states with the same scanning amplitude of 7 degrees. This might be because of factors accounted for, such as backlash in the gears of motors, inconsistency in the stepper motor rotation, and error in the identified elevation angle of the receiver photo-diode, which is used in the rotational transformation in generating motor commands. Such oscillations are further minimized by the adaptive scanning technique. Fig. 10 shows

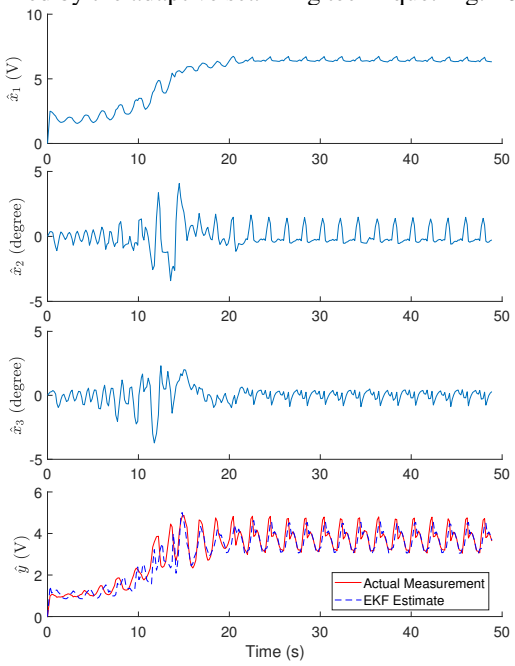

Fig. 9. Experimental results with constant scanning amplitude $\delta_r = 7^\circ$ under a constant disturbance $\kappa = 1^\circ/\text{s}$.

the plots for an experimental run when the adaptive scanning is implemented. It is observed that all of the estimates and the measurement converge to their respective steady state values with significantly smaller oscillations compared with the non-adaptive scanning case. The adaptive scanning also leads to reduced control effort, since when δ_r is low, the motor commands become smaller in each iteration.

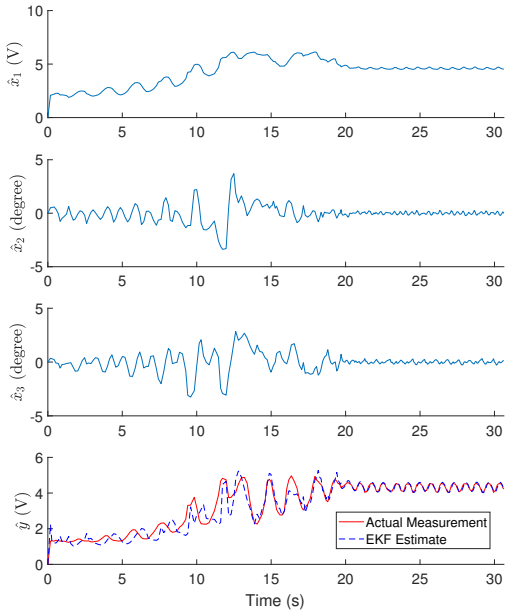

Fig. 10. Experimental results with adaptive scanning amplitude and disturbance $\kappa = 1^\circ/s$.

VII. CONCLUSIONS

In this work, an active alignment control method for LED-based optical communication system was proposed. With a light intensity model, the estimation problem was first formulated in the state-space domain. A circular scanning technique was introduced to take successive intensity measurements that were used in an EKF-based estimation algorithm. The estimates were then used by the PI controller to generate the control commands for alignment, which were later translated to the motor commands using the rotational transformation. The disturbance accounting for the unknown relative motion between the transmitter and the receiver was captured as part of a white Gaussian noise. Both in simulation and the experiments, the tracking efficacy of the method was verified in the presence of a constant disturbance. Furthermore, an adaptive strategy for the scanning amplitude was implemented, which was demonstrated to provide higher intensity measurement and consume lower energy at the steady state.

For future work, we first plan to implement this alignment algorithm on two receiver-transmitter modules to enable the bi-directional communication between them. Moving forward, the effectiveness of the proposed system will be explored in the underwater setting, which motivated the LED-based optical communication in the first place. In particular, we will mount the communication modules on two underwater robots, and investigate the improvement of the algorithm to address additional challenges introduced by water disturbances and robot motion.

ACKNOWLEDGEMENTS

This work was supported by National Science Foundation (IIS 1319602, ECCS 1446793, IIS 1734272). We like to thank Professor Hassan Khalil and Dhrubajit Chowdhary for their helpful discussions on the analysis and controller design for the system.

REFERENCES

[1] L. Butler, "Underwater radio communication," *Amateur Radio*, 1987.
[2] S. Climent, A. Sanchez, J. V. Capella, N. Meratnia, and J. J. Serrano, "Underwater acoustic wireless sensor networks: Advances and future trends in Physical, MAC and routing layers," *Sensors*, vol. 14, no. 1, p. 795, 2014.
[3] F. Hanson and S. Radic, "High bandwidth underwater optical communication," *Appl. Opt.*, vol. 47, no. 2, pp. 277–283, Jan 2008.
[4] R. Hagem, D. V. Thiel, S. O'Keefe, A. Wixted, and T. Fickenscher, "Low-cost short-range wireless optical FSK modem for swimmers feedback," in *Proceedings of 2011 IEEE Sensors Conference*, Oct 2011, pp. 258–261.
[5] F. Lu, S. Lee, J. Mounzer, and C. Schurgers, "Low-cost medium-range optical underwater modem: Short paper," in *Proceedings of the Fourth ACM International Workshop on UnderWater Networks*, ser. WUWNet '09. New York, NY, USA: ACM, 2009, pp. 11:1–11:4.
[6] H. Brundage., "Designing a wireless underwater optical communication system," Master's thesis, Massachusetts Institute of Technology, 2010.
[7] M. Doniec and D. Rus, "Bidirectional optical communication with AquaOptical II," in *Communication Systems (ICCS), 2010 IEEE International Conference on*, Nov 2010, pp. 390–394.
[8] C. Pontbriand, N. Farr, J. Ware, J. Preisig, and H. Popenoe, "Diffuse high-bandwidth optical communications," in *OCEANS 2008*, Sept 2008, pp. 1–4.
[9] D. Anguita, D. Brizzolara, and G. Parodi, "Building an underwater wireless sensor network based on optical ommunication: Research challenges and current results," in *Sensor Technologies and Applications, 2009. SENSORCOMM'09. Third International Conference on*. IEEE, 2009, pp. 476–479.
[10] ——, "Optical wireless communication for underwater wireless sensor networks: Hardware modules and circuits design and implementation," in *OCEANS 2010*. IEEE, 2010, pp. 1–8.
[11] I. Rust and H. Asada, "A dual-use visible light approach to integrated communication and localization of underwater robots with application to non-destructive nuclear reactor inspection," *Robotics and Automation (ICRA), 2012 IEEE International Conference on*, pp. 2445–2450, May 2012.
[12] J. Simpson, B. Hughes, and J. Muth, "Smart transmitters and receivers for underwater free-space optical communication," *Selected Areas in Communications, IEEE Journal on*, vol. 30, no. 5, pp. 964–974, June 2012.
[13] G. Soysal and M. Efe, "Kalman filter aided cooperative optical beam tracking," *Radioengineering*, pp. 242–248, June 2010.
[14] G. Marola, D. Santerini, and G. Prati, "Stability analysis of direct-detection cooperative optical beam tracking," *IEEE Transactions on Aerospace and Electronic Systems*, vol. 25, no. 3, pp. 325–334, May 1989.
[15] P. B. Solanki and X. Tan, "Experimental implementation of extended Kalman filter-based optical beam tracking with a single receiver," in *2016 IEEE International Conference on Advanced Intelligent Mechatronics*, July 2016, pp. 1103–1108.
[16] ——, "Extended Kalman filter-aided active beam tracking for LED communication in 3D space," in *ASME Dynamic Systems and Control Conference, accepted*, 2017.
[17] M. Doniec, M. Angermann, and D. Rus, "An end-to-end signal strength model for underwater optical communications," *Oceanic Engineering, IEEE Journal of*, vol. 38, no. 4, pp. 743–757, Oct 2013.
[18] K. Reif, S. Gunther, E. Yaz, and R. Unbehauen, "Stochastic stability of the discrete-time extended Kalman filter," *IEEE Transactions on Automatic Control*, vol. 44, no. 4, pp. 714–728, Apr 1999.